D-Band Perfect Anomalous Reflectors for 6G Applications

YUTO KATO [1], **(Member, IEEE), KOHEI OMORI** [2], **AND ATSUSHI SANADA** [2], **(Member, IEEE)**

[1]Research Institute for Physical Measurement, National Institute of Advanced Industrial Science and Technology, Tsukuba 305-8563, Japan
[2]Graduate School of Engineering Science, Osaka University, Toyonaka 560-0043, Japan

Corresponding author: Yuto Kato (y-katou@aist.go.jp)

ABSTRACT We demonstrate anomalous reflectors at 140 GHz for the application of 6G communication coverage expansion. The reflectors are designed on cyclo-olefin polymer (COP) substrates on the basis of measured complex permittivity and conductivity at millimeter frequencies obtained with the balanced-type circular disk resonator method. From full-wave simulations, we confirm that nearly perfect anomalous reflection characteristics are realized with suppressed parasitic reflections in undesired directions. The simulated efficiencies excluding the material losses of the reflectors designed with the reflection angle $\theta_R = 30°, 45°, 60°$, and $75°$ are 99.5%, 98.9%, 99.7%, and 99.8%, respectively. In addition, we fabricate the designed reflectors on the COP substrates and experimentally evaluate their anomalous reflection performances. The measured overall efficiencies of the reflectors with $\theta_R = 45°, 60°$, and $75°$ are 88.0%, 83.6%, and 81.6%, respectively. This is the first demonstration of highly efficient anomalous reflectors in the D-band.

INDEX TERMS Anomalous reflectors, coverage expansion, D-band, metasurfaces, millimeter-wave, reflection efficiency, 6G communication.

I. INTRODUCTION

Millimeter-waves above 100 GHz are supposed to be used in the sixth generation (6G) wireless communication to realize high-speed and large-capacity communication with performances far exceeding those of 5G [1]–[3]. Since the millimeter-waves are vulnerable to blockages by physical obstacles such as buildings and trees, narrowing of the service coverage becomes a more severe problem than in conventional microwave communications [4], [5]. One of the promising solutions for mitigating the coverage holes is using metasurface-based high efficiency reflectors with the anomalous reflection property in which a reflector reflects incident waves in a desired arbitrary direction different from the specular direction [6]–[13]. This leads to easy coverage designs with flexible reflector deployments on fixed walls and/or windows of buildings.

Metasurfaces are two-dimensional planar subwavelength structures and have been presented to achieve amplitude, wavefront, and polarization manipulations of the incoming electromagnetic wave in a wide frequency range from

The associate editor coordinating the review of this manuscript and approving it for publication was Zhongyi Guo.

microwaves to the optical region [14]–[19]. In general, it is possible to arbitrarily manipulate a reflection direction using a metasurface with controlled local reflection phase distributions [20]. So far, several metasurface-based anomalous reflectors have been demonstrated at microwave frequencies [21]–[26]. However, a reflector only with the local phase control suffers from parasitic reflections in unwanted directions as the reflection angle deviation from the specular direction increases [22], [23], [27], [28]. This leads to a deterioration of reflection efficiency.

Recently, a high efficiency anomalous reflector with suppressed parasitic reflections has been proposed by introducing in-plane energy propagations in a substrate along a metasurface based on nonlocal "active-lossy" design [6]. The design enables to introduce effective local gains and losses required for a perfect efficiency by utilizing in-plane energy propagations with a completely passive configuration. A nearly perfect anomalous reflector reflecting a normal incident wave into the reflection angle of 70° has been realized with the simulated efficiency of 99.7% excluding the material losses and the measured efficiency of 93.8% including the material losses at 8 GHz. However, there has been no demonstration of a high efficiency anomalous

reflector at millimeter-wave frequencies above 100 GHz for 6G applications where material losses are to be drastically increased.

In practice, the efficiency deterioration of an anomalous reflector is caused by two mechanisms: the energy leakage to the parasitic reflections and the material losses in a substrate (dielectric and conductor losses). In order to realize a high efficiency anomalous reflector at millimeter-wave frequencies, it is indispensable not only to suppress the parasitic reflections but also to appropriately select a low-loss substrate. In general, owing to the increased dielectric loss tangent and reduced conductivity, the choice of low-loss substrates in the millimeter-wave bands is much more limited than in the microwave bands. In particular, the effective conductivity of metallic layers on a dielectric substrate tends to become significantly smaller than the bulk metal value depending on the surface roughness since the skin depth becomes comparable to the surface roughness [29], [30]. However, there is a lack of reliable information of complex permittivity and conductivity of substrates in the millimeter-wave bands for appropriately selecting low-loss substrates. This also poses an accuracy problem in reflector designs.

Until recently, no high-precision material measurement technique has been established in the millimeter-wave bands above 100 GHz. Resonator methods [31]–[34] are promising for accurately measuring low-loss substrate materials. However, applying the resonator methods in the millimeter-wave bands above 100 GHz has been challenging due to machining difficulty of a tiny resonator. Recently, in contrast to conventional resonator methods utilizing the fundamental mode resonances, we have developed wideband material measurement technique for the complex permittivity and conductivity of substrate materials up to over 100 GHz with a single system by utilizing higher-order mode resonances of a balanced-type circular disk resonator (BCDR) [35]–[38]. This measurement technique provides reliable reflector designs based on accurately measured material parameters and reduces trial-and-error prototyping.

The technique is also highly useful for an appropriate selection of a substrate in the millimeter-wave bands. According to the material measurement results provided by the BCDR method [36]–[38], we have found that cyclo-olefin polymer (COP) is a promising low-loss substrate material in the millimeter-wave bands above 100 GHz because of its low relative permittivity, low loss tangent, and high conductivity of metallic layers on the substrate. High-conductive and high-strength metallic layers can be formed on the COP substrate without introducing a roughening treatment or adhesive layers [39].

In this paper, we demonstrate perfect anomalous reflectors in the D-band for the first time aimed at the application of 6G communication coverage expansion. We select the COP as the substrate material according to the precedent knowledge mentioned above. The reflectors are designed based on experimentally obtained material parameters of the COP substrate
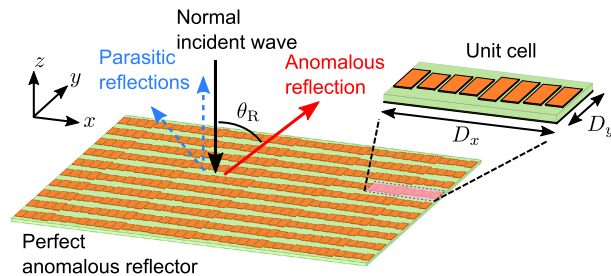
FIGURE 1. Perfect anomalous reflector consisting of a metallic patch array on a dielectric substrate backed by a metallic ground plane.

using the BCDR method in the millimeter-wave bands. The reflection performances of the designed anomalous reflectors are studied both numerically and experimentally. It is noted that the novelty and importance of this paper are not to propose a novel design theory but to demonstrate an application potential of anomalous reflectors for use in the 6G communication based on the design scheme already proposed in [6]. We achieve this goal with the approach of designing reflectors exploiting our recently developed high-precision material measurement technique in the millimeter-wave bands above 100 GHz.

The remainder of this paper is organized as follows. In Section II, we present the configuration of the perfect anomalous reflector. In Section III, four anomalous reflectors are designed at 140 GHz for normal incident waves with the refection angles of 30°, 45°, 60°, and 75° based on highly accurate material characterization. The reflection performances of the designed reflectors are numerically investigated in Section IV. Furthermore, the anomalous reflectors are fabricated, and the anomalous reflection characteristics are measured to evaluate the efficiencies in Section V. Finally, conclusions are presented in Section VI.

II. PERFECT ANOMALOUS REFLECTOR

Fig. 1 shows a perfect anomalous reflector consisting of a metallic patch array on a dielectric substrate backed by a metallic ground plane. Here, let the reflector be on the xy-plane in free space and illuminated with the y-polarized normal incident wave (incident angle $\theta_I = 0°$). By introducing a gradient in the reflection phase in the x-direction, one can change the reflection direction to the desired direction with the reflection angle θ_R. In general, in addition to the desired direction (θ_R), parasitic reflections occur in the specular (0°) and symmetric ($-\theta_R$) directions, which degrades the efficiency of the anomalous reflector especially for large θ_R. The efficiency can be drastically improved by introducing the nonlocal "active-lossy" design [6] based on unit cell optimizations.

III. MATERIAL CHARACTERIZATION-BASED DESIGN AND OPTIMIZATION

Here, we design perfect anomalous reflectors at 140 GHz based on the design methodology in [6] using actually measured material parameters obtained with our recently developed high-precision and broadband material characterization technique [36], [37].
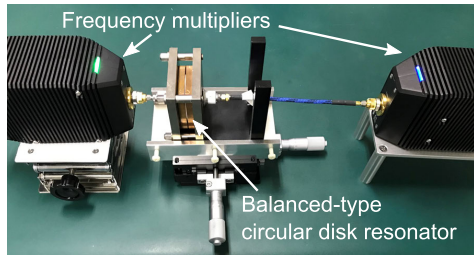
(a)
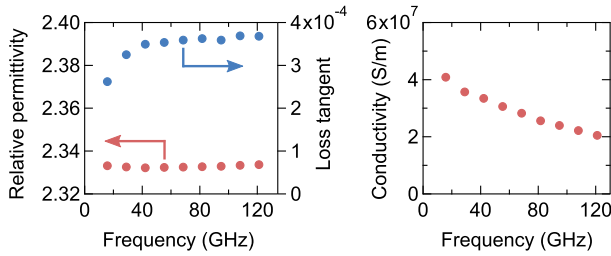
(b)

(c)

FIGURE 2. Material characterization of the COP substrate using the BCDR method. (a) Measurement system. Measurement results of (b) the complex permittivity and (c) conductivity.

A. MATERIAL CHARACTERIZATION OF SUBSTRATE

We first measure the complex permittivity of the substrate material and the conductivity of the metallic layers used for fabricating the reflectors. The thickness of the COP substrate is 0.1 mm. To suppress the conductivity degradation of the metallic layers, the metallic layers are formed on both sides of the substrate by plating 18 μm-thick copper after surface modification with ultraviolet irradiation without introducing a roughening treatment or adhesive layers [39]. We measure the complex permittivity and conductivity using the BCDR method (see Fig. 2(a)). Owing to the mode-selective behavior of the BCDR over a wide band, the BCDR method can provide broadband measurements of the material parameters over 10 octaves with a single resonator by utilizing higher-order TM_{0m0} mode resonances [36], [37]. Here, due to the limitations of the Keysight frequency multipliers N5295AX03 that generate the millimeter-waves, the transmission measurements of the resonator are carried out at frequencies up to 125 GHz for determining the material parameters of the COP substrate. Fig. 2(b) and (c) show the measurement results of the complex permittivity and conductivity, respectively, at the resonant frequencies ranging from 16 GHz to 121 GHz. It can be seen from the figures that the COP substrate has a low relative permittivity ($\epsilon_r < 2.4$), low loss tangent ($\tan\delta < 4 \times 10^{-4}$), and high conductivity ($\sigma > 2 \times 10^7$ S/m) with mild frequency dependences in the millimeter-wave bands. The COP substrate maintains relatively high conductivity in the millimeter-wave bands. It has been reported that the conductivity drops more significantly to $\sigma < 5 \times 10^6$ S/m in the millimeter-wave bands for certain substrates with a lossy seed layer [37]. These frequency dependences are difficult to be accurately predicted solely from the measurement results at microwave frequencies because they are affected by various factors

(a)

(b)
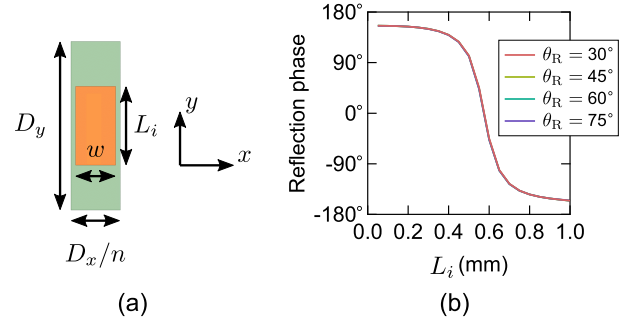
FIGURE 3. Metallic patch element that constitutes a unit cell of a perfect reflector. (a) Dimensional parameters of an element. (b) Relationship between the patch length L_i and the reflection phase at 140 GHz for the designs with $\theta_R = 30°$, 45°, 60°, and 75° (all almost identical).

including the intrinsic material properties and the geometric factors such as surface profiles of the dielectric and metallic layer especially in the millimeter-wave bands [29], [30]. According to Fig. 2(b) and (c), it is reasonable to predict the material parameters at 140 GHz from the ultra-wide band millimeter-wave measurement results with the extrapolations. The obtained estimates at 140 GHz are: relative permittivity $\epsilon_r = 2.33$, loss tangent $\tan\delta = 3.7 \times 10^{-4}$, and conductivity $\sigma = 2.0 \times 10^7$ S/m.

B. UNIT CELL OPTIMIZATION FOR PERFECT ANOMALOUS REFLECTION

Based on the material parameters obtained in the previous subsection, we design perfect anomalous reflectors at 140 GHz for $\theta_R = 30°$, 45°, 60°, and 75°. The numbers of the metallic patch elements in the unit cell along the x-direction (see Fig. 1) are chosen to be $n = 10$, 8, 8, and 6 for $\theta_R = 30°$, 45°, 60°, and 75°, respectively. According to the design methodology in [6], the periods of the unit cell in the x- and y-directions are determined by $D_x = \lambda_0/\sin\theta_R$ and $D_y = \lambda_0/2$, respectively, where $\lambda_0 = 2.14$ mm is the free space wavelength at 140 GHz.

The dimensional parameters of the element are shown in Fig. 3(a). The widths of the metallic patches are chosen to be $w = 0.35$ mm, 0.31 mm, 0.25 mm, and 0.37 mm for $\theta_R = 30°$, 45°, 60°, and 75°, respectively. The patch lengths L_i ($i = 1, \cdots, n$) are optimized numerically for achieving the desired perfect anomalous reflections: first, we calculate the relationship between the length L_i and the local reflection phase of the element for a normal incident wave at 140 GHz by full-wave simulations using the HFSS driven solver under 2-D periodic boundary conditions. Fig. 3(b) shows the results. It is seen from the figure that the reflection phase responses are nearly equal for all the element designs corresponding to various θ_R regardless of different values of (n, D_x, w). Based on the relations of Fig. 3(b), the initial estimate of each L_i is given for the optimization so that the local reflection phase coincides with the phase of R in the following equation:

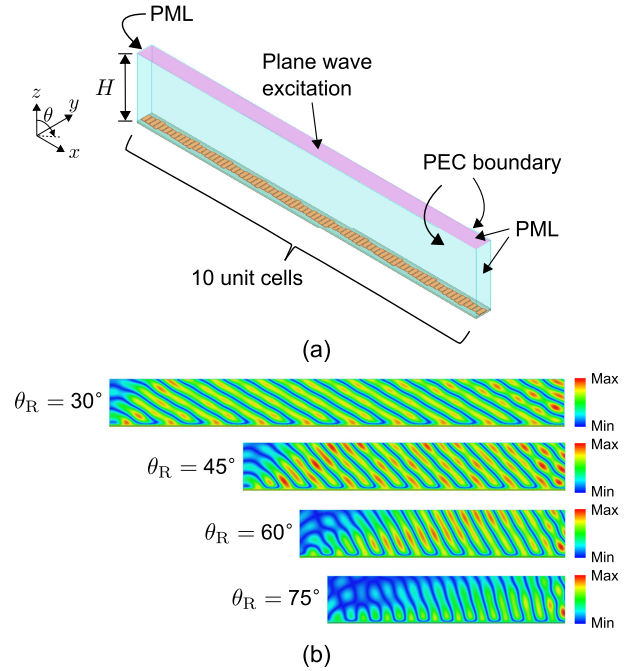$$R(x_i) = \frac{Z_s(x_i) - \eta_0}{Z_s(x_i) + \eta_0}, \tag{1}$$

(a)

(b)

(c)
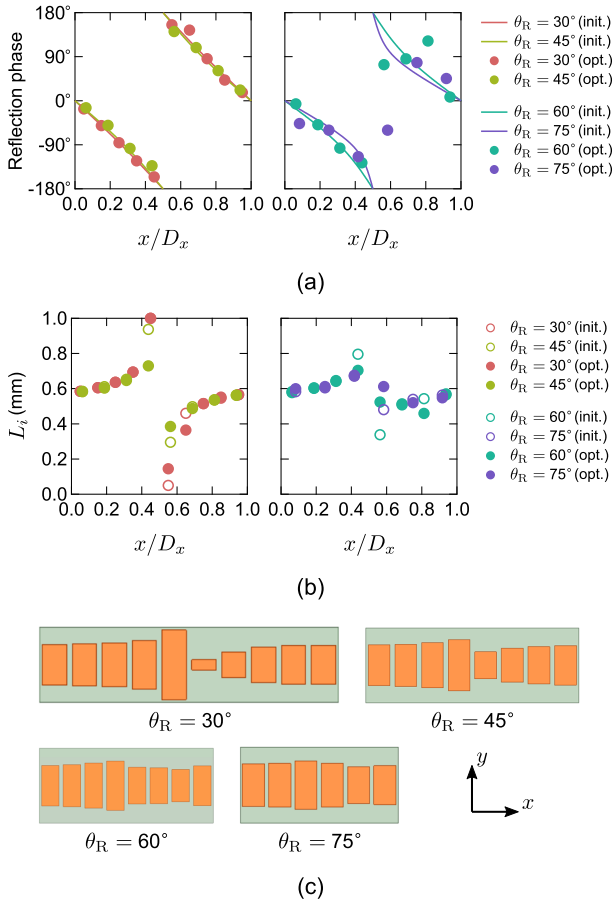
FIGURE 4. Unit cell optimization for the perfect anomalous reflection. (a) Reflection phase distributions on the unit cell before and after the optimization. (b) Patch lengths L_i in the unit cell before and after the optimization. (c) Optimized unit cells of the perfect anomalous reflectors for $\theta_R = 30°$, $45°$, $60°$, and $75°$.

(a)

(b)

FIGURE 5. Simulations of the perfect anomalous reflection characteristics. (a) Configurations of the simulations. (b) Simulated reflected electric field distributions for the reflectors with $\theta_R = 30°$, $45°$, $60°$, and $75°$ (linear scale).
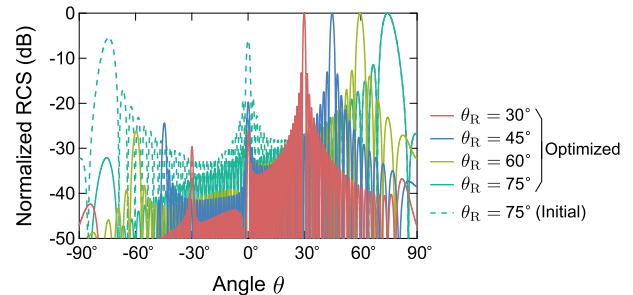
FIGURE 6. Normalized bistatic radar cross sections (RCSs) calculated for the reflectors consisting of 30 unit cells. The RCSs are offset to set the peak amplitudes be 0 dB.

where x_i is the x-coordinate of the center of the i-th element, η_0 is the wave impedance in free space, and Z_s is the surface impedance of a perfect anomalous reflector in an ideal design consisting of a periodic array of lossy and gain unit cells [27], [40] given by

$$Z_s(x_i) = \frac{\eta_0}{\sqrt{\cos\theta_R}} \frac{\sqrt{\cos\theta_R} + \exp\left(-jk_0 x_i \sin\theta_R\right)}{1 - \sqrt{\cos\theta_R} \exp\left(-jk_0 x_i \sin\theta_R\right)}. \quad (2)$$

Here, k_0 is the wavenumber in free space. The reflection phases of (1) are shown as solid lines in Fig. 4(a), and the corresponding initial estimates of L_i obtained from Fig. 3(b) are shown as unfilled markers in Fig. 4(b).

Then, all L_i are optimized by calculating the reflection coefficients of the diffraction modes of the unit cell at the Floquet port by full-wave simulations under 2-D periodic boundary conditions. Here, to maximize the reflection from the normal incident wave to the desired anomalous reflection, corresponding to the reflection between the 0th and 1st diffraction modes in our configuration, we set the optimization goal as $\left|S_{11}^{0\to1}\right| = 1$, where $S_{11}^{i\to j}$ is the reflection coefficient between the i-th and j-th modes. The optimized L_i values are shown as filled markers in Fig. 4(b), and the

local reflection phases of the elements calculated from the optimized L_i values using the relations of Fig. 3(b) are shown as filled markers in Fig. 4(a). It is seen from Fig. 4(a) that the optimized local reflection phases deviate from the initial values due to the nonlocal "active-lossy" behavior. Fig. 4(c) shows the optimized unit cells of the perfect anomalous reflectors for $\theta_R = 30°$, $45°$, $60°$, and $75°$.

IV. REFLECTOR PERFORMANCE
Here, we present performances of the designed anomalous reflectors evaluated by numerical simulations.

A. ANOMALOUS REFLECTION CHARACTERISTICS
We first visualize anomalous reflection characteristics of the designed reflectors obtained by full-wave simulations using HFSS driven solver. In the simulations, a chain of 10 unit cells periodically arranged in the x-direction is prepared in the analysis space with $H = 2\lambda_0 = 4.28$ mm, and

a *y*-polarized normal incident plane wave is introduced from the +*z*-direction, as shown in Fig. 5(a). The boundaries parallel to the *zx*-plane of the analysis space are set to be perfect electric conductors (PECs) in order to mimic an infinite periodic reflector in the *y*-direction. The other boundaries are configured to be with the perfectly matched layers (PMLs). Fig. 5(b) shows the simulated electric field distributions for the scattered wave in the *zx*-plane calculated at 140 GHz for the designed reflectors with $\theta_R = 30°$, $45°$, $60°$, and $75°$. As seen in the figure, most of the incident powers are reflected toward the desired directions.

To quantitatively evaluate the reflection characteristics, the bistatic radar cross sections (RCSs) are calculated by the full-wave simulations for each reflector illuminated by a normal incident wave from the +*z*-direction at the Floquet port under the 2-D periodic boundary conditions in the *x*- and *y*-directions. By using the reflected wave distributions from each unit cell obtained from the simulations, the bistatic RCSs for the reflectors consisting of 30 unit cells periodically arranged in the *x*-direction are calculated. The results are shown in Fig. 6. In the figure, the RCSs are offset to set the peak amplitudes be 0 dB to clearly see the parasitic reflection levels for the reflectors with the different aperture sizes. As seen from Fig. 6, the peak positions of the RCS main lobes are 29.9°, 44.8°, 59.7°, and 74.3°, which agree well with the corresponding design values of θ_R. The parasitic reflection levels are suppressed below −20 dB for all the designs thanks to the nonlocal "active-lossy" design. For instance, for the design of $\theta_R = 75°$, the parasitic reflection levels in the specular (0°) and symmetric (−75°) directions are as small as −23.2 dB and −32.0 dB, respectively, It is noted that the beamwidths increase with increasing θ_R due to the aperture size reduction (see Fig. 5(b)).

For a comparative purpose, we carry out additional simulations for the reflector with initial L_i values based on the local reflection phase of (1) for $\theta_R = 75°$ without optimizations. The bistatic RCS for the initial design is shown in Fig. 6 with a dashed line. By comparing the results for the initial and optimized designs of $\theta_R = 75°$, it is found that the unit cell optimization significantly drops the parasitic reflections in the specular (0°) and symmetric (−75°) directions by 17.3 dB and 26.6 dB, respectively, which leads to a considerable increase in the reflection efficiency to the desired direction (75°) as will be clarified in the next subsection.

Fig. 7 shows the distributions of the real parts of the Poynting vectors on the unit cell boundary parallel to the *zx*-plane calculated for the reflectors with $\theta_R = 75°$ after and before optimizations. As seen from the figure, the amplitude of the power flow is modulated in the *xz*-plane with a flat wavefront for the optimized reflector, which implies that the reflected power flows only in one direction with suppressed parasitic reflections. The angle of the modulation θ_P (see Fig. 7(a)) is given from [6]

$$\tan \theta_P = \frac{\sin \theta_R}{1 + \cos \theta_R}. \tag{3}$$
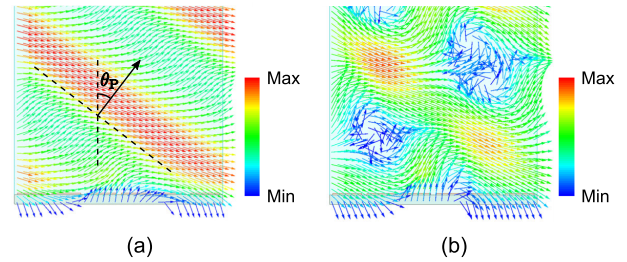

FIGURE 7. Distributions of the real parts of the Poynting vectors on the unit cell boundary parallel to the *zx*-plane calculated for the reflectors with $\theta_R = 75°$ (a) after and (b) before the optimization (linear scale).

For the case with $\theta_R = 75°$, θ_P is calculated as 37.5°, which is in good agreement with the simulated results of Fig. 7(a) and supports the fact that the reflected power flows in the desired direction. It is also seen from the figure that the unit cell has both areas with incoming and outgoing power flows from/to free space, implying the nonlocal "active-lossy" operation with an in-plane wave excitation in the substrate.

B. REFLECTION EFFICIENCY
The efficiency of the anomalous reflection is quantitatively evaluated from the simulations by calculating the mode conversion efficiency between the 0th and 1st modes, $\left| S_{11}^{0 \to 1} \right|^2$, for the designed reflectors. The simulated efficiencies for the optimized designs of $\theta_R = 30°$, $45°$, $60°$, and $75°$ are shown in Fig. 8 as red markers. It can be seen from the figure that the reflection efficiency of $\theta_R = 30°$ is as high as 95.3%. The efficiency slightly decreases as the reflection angle θ_R increases, yet a high efficiency of 88.6% is maintained even at $\theta_R = 75°$. In contrast, blue markers in Fig. 8 show the efficiencies for the initial designs based on the local reflection phase of (1) without optimizations. The efficiency of the initial designs decreases significantly with the reflection angle and deteriorates to as low as 65.8% at $\theta_R = 75°$, which is due to the increase in inevitable parasitic reflections by the local phase control design (as in the specular and symmetric directions in Fig. 6). The optimized designs enable for the efficiency to drastically exceed this limitation of the initial designs.

As mentioned in Introduction, the total loss of each reflector is caused by two mechanisms: the energy leakage to the parasitic reflections and the material losses in the substrate (dielectric and conductor losses). The former and latter contributions are numerically evaluated by calculating $\sum_{i \neq 1} \left| S_{11}^{0 \to i} \right|^2$ and $\left(1 - \sum_i \left| S_{11}^{0 \to i} \right|^2\right)$, respectively. Note that $\sum_i \left| S_{11}^{0 \to i} \right|^2$ corresponds to the total amount of reflections in all the allowed directions. Fig. 9 shows the contributions of the two loss mechanisms for the optimized designs. As seen in the figure, most of the total loss is attributed to the material losses and the contribution of the parasitic reflections is almost negligible ranging from 0.2% to 1.0% depending on the designs. Therefore, the total efficiency of each reflector depends much on the characteristics of the substrate, suggesting the importance of an appropriate low-loss substrate
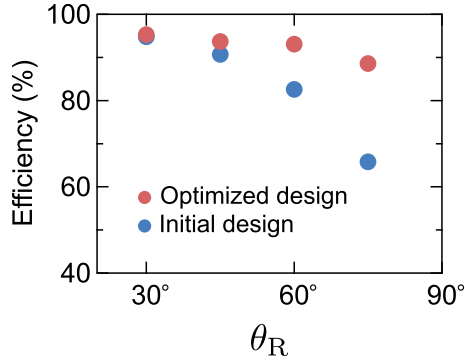
FIGURE 8. Efficiency of anomalous reflectors before and after the unit cell optimizations.
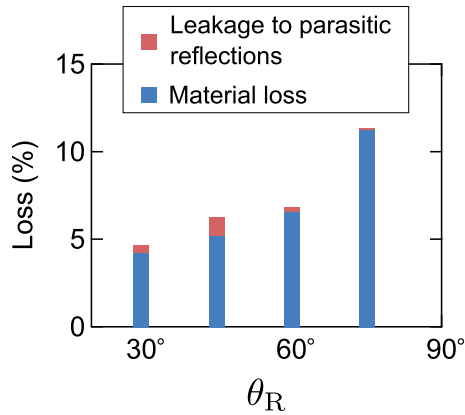

FIGURE 9. Contributions of the two loss mechanisms for the optimized designs of perfect anomalous reflectors.
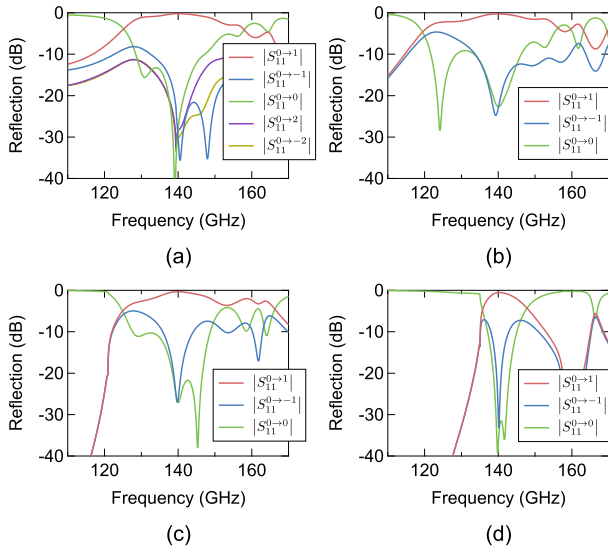

FIGURE 10. Frequency dependences of $\left|S_{11}^{0 \to i}\right|$ for each reflector design. Results for (a) $\theta_R = 30°$, (b) $\theta_R = 45°$, (c) $\theta_R = 60°$, and (d) $\theta_R = 75°$.

material selection. The efficiencies excluding the material losses for $\theta_R = 30°, 45°, 60°$, and $75°$ are calculated to be $99.5\%, 98.9\%, 99.7\%$, and 99.8%, respectively. Thus, except for practically unavoidable material losses, almost perfect anomalous reflectors are designed even for large reflection angles.
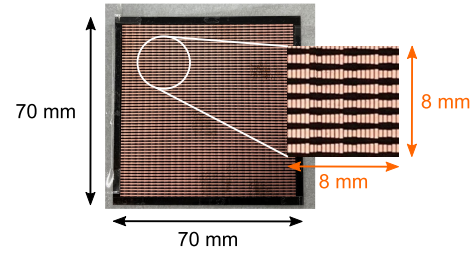

FIGURE 11. Photograph of the prototype with $\theta_R = 60°$.

Fig 10 shows frequency dependences of $\left|S_{11}^{0 \to i}\right|$ for each reflector design. It is noted that there are 5 propagating diffraction modes for the reflector with $\theta_R = 30°$, whereas the other reflectors have 3 propagating diffraction modes depending on D_x. In Fig. 10, the maximum value of the red trace ($\left|S_{11}^{0 \to 1}\right|$) at 140 GHz corresponds to the efficiency of each reflector shown in Fig. 8. As seen from Fig. 10, the frequency bandwidth of the anomalous reflection decreases with increasing θ_R, and the fractional bandwidths calculated from the 3-dB bandwidth of $\left|S_{11}^{0 \to 1}\right|$ are $22.0\%, 24.7\%, 17.3\%$, and 7.6%, for $\theta_R = 30°, 45°, 60°$, and $75°$, respectively. It is noted that the reflection angle shifts with the frequency according to $\theta_R = \sin^{-1}(c/fD_x)$ as in the beam squinting [41], where f is the frequency and c is the speed of light.

Although the cause of the efficiency and bandwidth degradations with increasing the reflection angle is not clear, let us give an intuitive physical interpretation: For an ideal design consisting of a periodic array of lossy and gain unit cells based on (2), except for extreme reflection angles larger than a specific value (80.1° in this case according to (1)), the local reflection amplitude at $x_i = D_x/2$ increases remarkably as the reflection angle increases. This suggests that the energy redistribution by in-plane wave propagations along the substrate is accelerated as the reflection angle increases in the optimized designs, which possibly results in the increase in the material losses in the substrate. A subtle unit cell optimization in the accelerated energy redistribution may narrow the bandwidth.
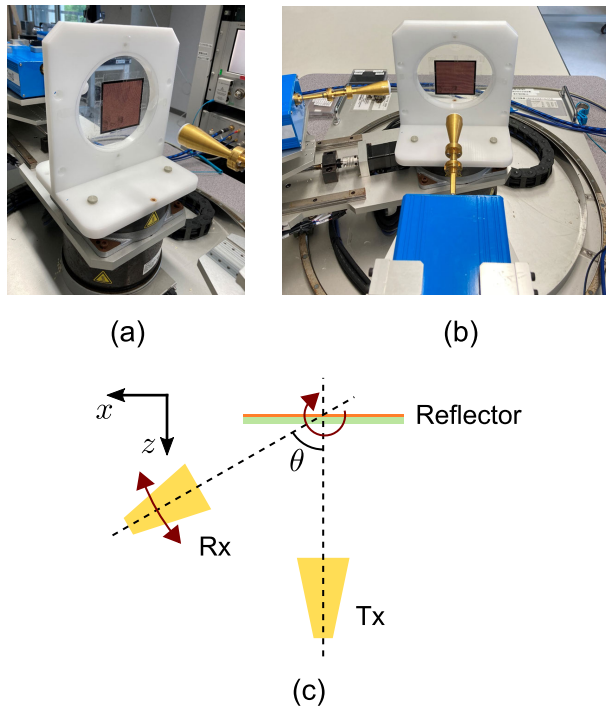
V. EXPERIMENTS
A. PROTOTYPE
The designed reflectors for $\theta_R = 45°, 60°$, and $75°$ are fabricated to experimentally demonstrate the anomalous reflection characteristics. By using standard printed circuit board lithography techniques with a typical tolerance of ± 0.02 mm, the prototypes are fabricated on the 0.1 mm-thick COP substrates with 18 μm-thick copper metallic patterns. The total size of each prototype is 70 mm × 70 mm. A photograph of a typical prototype for $\theta_R = 60°$ is shown in Fig. 11.

B. MEASUREMENT SYSTEM AND PROCEDURE
Fig. 12 shows the experimental system developed for this study. Two identical D-band corrugated lens horn antennas with a 28 dBi gain are used in the system. The diameter of the dielectric collimation lenses is 24 mm. The distance between each antenna and the reflector is 107 mm (= $50\lambda_0$).

FIGURE 12. Experimental system. Photographs of the experimental setups for measuring (a) normal and (b) oblique reflections. (c) Schematic of the experimental system. For the normal reflection, the direct reflection is measured using a single antenna.

The full-width at half-maximum (FWHM) of the beam at the sample position is approximately 13 mm that is much smaller than the sample size, so the scattering from the sample holder is considered to be negligible. As shown in Fig. 12(c), one antenna (Tx) is fixed so that the reflector is illuminated normally, and the other antenna (Rx) rotates around the sample with an automated rotation stage. S-parameters between the antennas are measured in the frequency range from 110 GHz to 170 GHz by a Keysight vector network analyzer (VNA) E8361A with OML frequency multipliers V06VNA2-T/R.

Before the measurements, the through-reflect-line (TRL) calibration [42] is performed for the VNA by facing the two antennas in line with the distance of 214 mm using linear automated stages. After the calibration, the reflector is placed on the sample holder and the reflection angle θ dependencies of the reflection for the normal incident waves are measured. The scanning range of θ in the measurements is limited to $90° \geq \theta \geq 40°$, and $-40° \geq \theta \geq -90°$ due to the collision of the frequency multipliers. For the specular reflection (0°), the direct reflection is measured using a single antenna (see Fig. 12(a)). In the measurements, the time domain gating is performed on the measured frequency domain S-parameter data in order to remove residual errors after the calibration originated from multiple reflections between the antennas [42].
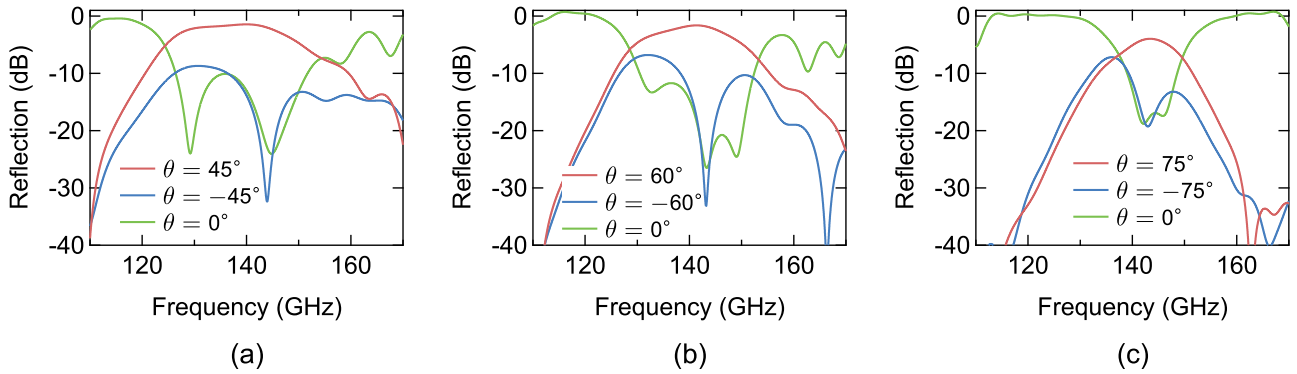
C. RESULTS AND DISCUSSION
Fig. 13 shows the measured reflections of the three reflectors in the three particular directions of $\theta = +\theta_R$, $-\theta_R$, and 0°. The reflection to $\theta = +\theta_R$ corresponds to the

desired anomalous reflection, whereas those to $\theta = -\theta_R$ and 0° correspond to the parasitic reflections in the symmetric and specular directions, respectively. As seen in the figure, most of the reflected powers are directed to the desired $+\theta_R$ directions with drastic parasitic reflection suppressions around 140 GHz. The total parasitic reflection power is minimized for each prototype at 144.2 GHz, 143.2 GHz, and 142.6 GHz for $\theta_R = 45°$, 60°, and 75°, respectively. At these frequencies, the reflection levels in the designed $+\theta_R$ directions are -2.1 dB, -1.8 dB, and -4.0 dB with the total parasitic reflections of -22.8 dB, -25.6 dB, and -15.8 dB for the designs of $\theta_R = 45°$, 60°, and 75°, respectively. The frequency shifts from 140 GHz are considered to be due to prototyping errors in fabrications. From these results, the anomalous reflection characteristics are experimentally demonstrated.

As for the frequency bandwidths of the anomalous reflections, the fractional 3-dB bandwidths of the reflections in the $+\theta_R$ directions calculated from Fig. 13 are 17.4%, 13.9%, and 8.4% for $\theta_R = 45°, 60°$, and 75°, respectively. The bandwidth decreases with increasing θ_R, which is also predicted in the simulated results of Fig. 10.

Fig. 14(a) shows the measured angle dependencies of the reflections at 144.2 GHz, 143.2 GHz, and 142.6 GHz, at which the total parasitic reflection powers are minimized, for the prototypes with $\theta_R = 45°$, 60°, and 75°. The reflections in $-40° < \theta < 40°$ are not measured to avoid the collision of the frequency multipliers. As seen from the figure, the reflection peaks near $+\theta_R$ reach -0.3 dB, -0.9 dB, and -3.5 dB for $\theta_R = 45°$, 60°, and 75°, respectively. The parasitic reflections in $-\theta_R$ directions are lower than the main reflection lobes by 30.5 dB, 32.2 dB, and 15.6 dB for $\theta_R = 45°$, 60°, and 75°, respectively, which attributes to high efficiencies of the anomalous reflections. In the range of $-90° \leq \theta \leq -40°$, the maximum side lobe levels are -30.1 dB, -20.9 dB, and -5.5 dB for the results of $\theta_R = 45°$, 60°, and 75°, respectively, demonstrating their directive reflection characteristics.

It is noted that, for the reflector with $\theta_R = 75°$, a relatively large side lobe with the level of -5.5 dB having a wide beam width is observed at the angle of $-58.0°$ away from the designed $-\theta_R$. The result is mainly due to the narrow incident beam width and does not directly reflect the reflection characteristics of the prototype in Fig. 6. To investigate the effect of the narrow spot size, additional full-wave simulations are carried out with the same configuration as in Fig. 5(a) except that an incident plane wave is replaced by a y-polarized normal incident gaussian beam with the FWHM of 13 mm to mimic the experimental setup. Fig. 14(b) shows the simulated directivities for the three reflector designs at 140 GHz. In contrast to the simulated RCSs of Fig. 6 for the reflectors illuminated by an infinitesimal plane wave, the side lobe positions shift to shallower angles than $-\theta_R$ with higher levels than those in Fig. 6. These results are qualitatively consistent with the experimental results of Fig. 14(a). If both the spot size and sample size are sufficiently large, such
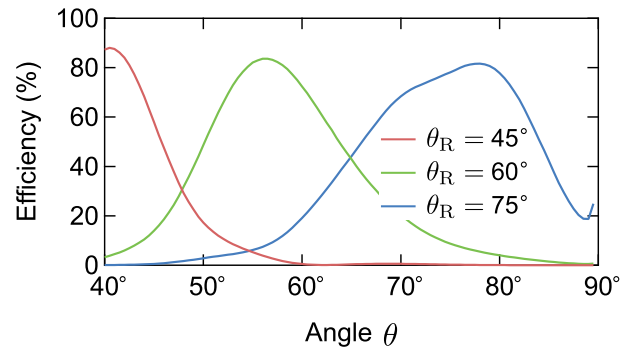
FIGURE 13. Measured reflections in the three directions of $\theta = +\theta_R$, $-\theta_R$, and $0°$. The reflection to $\theta = +\theta_R$ corresponds to the desired anomalous reflection, whereas those to $\theta = -\theta_R$ and $0°$ correspond to the parasitic reflections in the symmetric and specular directions, respectively. (a) $\theta_R = 45°$. (b) $\theta_R = 60°$. (c) $\theta_R = 75°$.
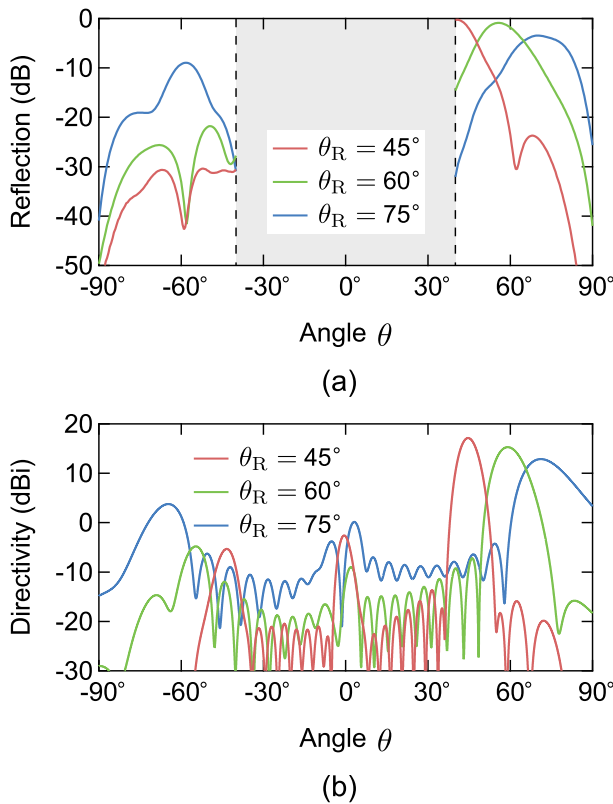
FIGURE 14. Angle dependencies of the reflections of the three reflectors. (a) Measured reflections in the angles θ ranging from $40°$ to $90°$ and from $-40°$ to $-90°$ for the prototypes with $\theta_R = 45°$, $60°$, and $75°$ at 144.2 GHz, 143.2 GHz, and 142.6 GHz, respectively. (b) Simulated directivities at 140 GHz.

FIGURE 15. Reflection efficiencies of the prototypes with $\theta_R = 45°$, $60°$, and $75°$ measured at the operating frequencies of 144.2 GHz, 143.2 GHz, and 142.6 GHz, respectively.

as in an actual use environment where a large reflector is illuminated from a distant base station antenna, the reflection characteristics of the reflectors will approach the desired ones of Fig. 6.

Further, the reflection efficiencies of the three prototypes are estimated from the measured reflections at each reflection angle. In the measurements, the amplitudes are normalized by the transmissions between the antennas without a sample by the TRL calibration. This can omit the normalization process for the efficiency evaluation used in [6] using specular reflections by a metallic plate that may have a finite

conductivity effect in the millimeter-wave bands. Then, the effect of the angle dependency of the cross-section is compensated with the correction factor $1/\xi$, where ξ is the ratio between amplitudes of reflections from an ideal perfect anomalous reflector and those of transmissions without a sample theoretically calculated under the physical optics approximation [6]. In the analysis, we take into account the beam spot size (≈ 13 mm), in contrast to the assumption in [6] where the entire sample size is illuminated by a plane wave. The obtained reflection efficiencies of the three prototypes at their operating frequencies are shown in Fig. 15. As seen from the figure, the efficiencies at the peak positions reach 88.0%, 83.6%, and 81.6% for $\theta_R = 45°$, $60°$, and $75°$, respectively. The measured efficiencies are slightly lower than the simulated values in Fig. 8 due to prototyping errors and experimental limitations; however, highly efficient anomalous reflectors are realized even for large reflection angles. For example, the measured efficiency for $\theta_R = 75°$ of 81.6% is significantly higher than that for the initial design of 65.8% (see Fig. 8). It is noted that, although the peak positions for the efficiencies of $\theta = 40.5°$, $56.0°$, and $78.0°$ are deviated from the designed values of $\theta_R = 45°$, $60°$, and $75°$, respectively, the deviations originate from this specific measurement system including the finite beam spot size as well as the increases in the operating frequencies and a possible misalignment of the measurement system.

TABLE 1. Performances of the D-band anomalous reflectors. For reference, performances of previously reported anomalous reflectors in the microwave bands are also shown.

	Design frequency	Incident angle θ_I	Reflection angle θ_R	Measured efficiency
This study	140 GHz	0°	45°	88.0%
			60°	83.6%
			75°	81.6%
Ref. [6]	8 GHz	0°	70°	93.8%
Ref. [22]	10 GHz	0°	28°	99.3%
			38°	93.6%
			48°	96.5%
			70°	91.2%
Ref. [23]	10 GHz	0°	70°	60.0%
Ref. [25]	20 GHz	10°	70°	98.7%
Ref. [24]	25 GHz	70°	10°	96.1%*

* Estimated efficiency excluding material losses in the reflector.

Table 1 summarizes the performances of the D-band anomalous reflectors in this study. For reference, performances of previously reported anomalous reflectors in the microwave bands found in the literature [6], [22]–[25] are also presented in Table 1. To the authors' best knowledge, no literature is found to compare efficiencies in the D-band. The efficiencies of the D-band anomalous reflectors are slightly lower than those reported at microwave frequencies. As shown in the simulated results of Fig. 9, the efficiency degradation of our anomalous reflectors is mostly due to their increased material losses originated from the dielectric and conductor losses. In particular, the conductor loss is drastically increased in the D-band due to the reduced conductivity because the skin depth becomes on the submicron order and comparable to the surface roughness. Therefore, the effective conductivity of metallic layers is drastically decreased compared to that in the microwave bands. For instance, the conductivity of the COP substrate is decreased to 34% of the bulk copper conductivity of 5.8×10^7 S/m in the D-band (see Fig. 2(b)). Even more significant degradation occurs for other substrates with a lossy seed layer used in a mounting process [37]. Incidentally, numerically calculated efficiencies of the designed reflectors using the bulk copper conductivity increase to 95.5%, 95.4%, and 92.4% for $\theta_R = 45°$, 60°, and 75°, respectively. These values are higher than the measured values in Table 1 and the simulated values in Fig. 8 and are comparable to the literature values in the microwave bands in Table 1.

This study presents the first demonstration of highly efficient anomalous reflectors in the D-band.

VI. CONCLUSION
We have demonstrated the anomalous reflectors at 140 GHz for the 6G applications. We have introduced reliable designs of the reflectors based on our recently developed high-precision material measurement technique in the millimeter-wave bands using the BCDR. With the unit cell optimization, the designed anomalous reflectors possess high efficiencies even at large reflection angles up to $\theta_R = 75°$. The designed reflectors have been fabricated on the COP substrate. The measured overall efficiencies including the material losses of the fabricated reflectors with $\theta_R = 45°$, 60°, and 75° are 88.0%, 83.6%, and 81.6%, respectively, with suppressed parasitic reflections in the undesired directions. The presented D-band anomalous reflectors have a potential to be used for a communication coverage expansion in the 6G communication. Future research includes expanding the operating frequency of anomalous reflectors up to 300 GHz.

REFERENCES
[1] L. Matti and L. Kari, "Key drivers and research challenges for 6G ubiquitous wireless intelligence," 6G Flagship, Oulu, Finland, White Paper, 2019. [Online]. Available: http://jultika.oulu.fi/files/isbn9789526223544.pdf

[2] Z. Zhang, Y. Xiao, Z. Ma, M. Xiao, Z. Ding, X. Lei, G. K. Karagiannidis, and P. Fan, "6G wireless networks: Vision, requirements, architecture, and key technologies," *IEEE Veh. Technol. Mag.*, vol. 14, no. 3, pp. 28–41, Sep. 2019.

[3] W. Saad, M. Bennis, and M. Chen, "A vision of 6G wireless systems: Applications, trends, technologies, and open research problems," *IEEE Netw.*, vol. 34, no. 3, pp. 134–142, May/Jun. 2020.

[4] A. Gómez-Andrades, R. Barco, and I. Serrano, "A method of assessment of LTE coverage holes," *EURASIP J. Wireless Commun. Netw.*, vol. 2016, no. 1, pp. 1–12, Dec. 2016.

[5] C. K. Anjinappa and I. Guvenc, "Coverage hole detection for mmWave networks: An unsupervised learning approach," *IEEE Commun. Lett.*, vol. 25, no. 11, pp. 3580–3584, Nov. 2021.

[6] A. Díaz-Rubio, V. S. Asadchy, A. Elsakka, and S. A. Tretyakov, "From the generalized reflection law to the realization of perfect anomalous reflectors," *Sci. Adv.*, vol. 3, no. 8, Aug. 2017, Art. no. e1602714.

[7] Y. Ra'di, D. L. Sounas, and A. Alù, "Metagratings: Beyond the limits of graded metasurfaces for wave front control," *Phys. Rev. Lett.*, vol. 119, no. 6, Aug. 2017, Art. no. 067404.

[8] C. Liaskos, S. Nie, A. Tsioliaridou, A. Pitsillides, S. Ioannidis, and I. Akyildiz, "A new wireless communication paradigm through software-controlled metasurfaces," *IEEE Commun. Mag.*, vol. 56, no. 9, pp. 162–169, Sep. 2018.

[9] W. Qingqing and Z. Rui, "Towards smart and reconfigurable environment: Intelligent reflecting surface aided wireless network," *IEEE Commun. Mag.*, vol. 58, no. 1, pp. 106–112, Jan. 2019.

[10] N. S. Perovic, M. D. Renzo, and M. F. Flanagan, "Channel capacity optimization using reconfigurable intelligent surfaces in indoor mmWave environments," in *Proc. IEEE Int. Conf. Commun. (ICC)*, Jun. 2020, pp. 1–7.

[11] Y. Cao, T. Lv, and W. Ni, "Intelligent reflecting surface aided multi-user mmWave communications for coverage enhancement," in *Proc. IEEE 31st Annu. Int. Symp. Pers., Indoor Mobile Radio Commun.*, Aug. 2020, pp. 1–6.

[12] M. Di Renzo, F. Habibi Danufane, X. Xi, J. de Rosny, and S. Tretyakov, "Analytical modeling of the path-loss for reconfigurable intelligent surfaces—Anomalous mirror or scatterer?" in *Proc. IEEE 21st Int. Workshop Signal Process. Adv. Wireless Commun. (SPAWC)*, May 2020, pp. 1–5.

[13] C. K. Anjinappa, F. Erden, and I. Guvenc, "Base station and passive reflectors placement for urban mmWave networks," *IEEE Trans. Veh. Technol.*, vol. 70, no. 4, pp. 3525–3539, Apr. 2021.

[14] J. Burch, J. Ma, R. I. Hunter, S. A. Schulz, D. A. Robertson, G. M. Smith, J. Wang, and A. Di Falco, "Flexible patches for mm-wave holography," *Appl. Phys. Lett.*, vol. 115, no. 2, Jul. 2019, Art. no. 021104.

[15] W. Wang, C. Guo, J. Tang, Z. Zhao, J. Wang, J. Sun, F. Shen, K. Guo, and Z. Guo, "High-efficiency and broadband near-infrared bi-functional meta-surface based on rotary different-size silicon nanobricks," *Nanomaterials*, vol. 9, no. 12, p. 1744, Dec. 2019.

[16] K. Cheng, Z. Hu, Y. Wang, J. Ma, and J. Wang, "High-performance terahertz vortex beam generator based on square-split-ring metasurfaces," *Opt. Lett.*, vol. 45, no. 21, pp. 6054–6057, 2020.

[17] W. Wang, Z. Zhao, C. Guo, F. Shen, J. Sun, and Z. Guo, "Irrotational nanobricks based high-efficiency polarization-independence meta-surfaces," *IEEE Photon. J.*, vol. 12, no. 4, pp. 1–8, Aug. 2020.

[18] W. Wang, R. Zhao, S. Chang, J. Li, Y. Shi, X. Liu, J. Sun, Q. Kang, K. Guo, and Z. Guo, "High-efficiency spin-related vortex metalenses," *Nanomaterials*, vol. 11, no. 6, p. 1485, Jun. 2021.

[19] H. Ai, Q. Kang, W. Wang, K. Guo, and Z. Guo, "Multi-beam steering for 6G communications based on graphene metasurfaces," *Sensors*, vol. 21, no. 14, p. 4784, Jul. 2021.

[20] N. Yu, P. Genevet, M. A. Kats, F. Aieta, J.-P. Tetienne, F. Capasso, and Z. Gaburro, "Light propagation with phase discontinuities: Generalized laws of reflection and refraction," *Science*, vol. 334, no. 6054, pp. 333–337, Oct. 2011.

[21] A. M. H. Wong and G. V. Eleftheriades, "Perfect anomalous reflection with a bipartite Huygens' metasurface," *Phys. Rev. X*, vol. 8, no. 1, Feb. 2018, Art. no. 011036.

[22] H. B. Jing, Q. Ma, G. D. Bai, and T. J. Cui, "Anomalously perfect reflections based on 3-bit coding metasurfaces," *Adv. Opt. Mater.*, vol. 7, no. 9, May 2019, Art. no. 1801742.

[23] N. A. Islam and S. Choi, "Compact folded dipole metasurface for high anomalous reflection angles with low harmonic levels," *Sci. Rep.*, vol. 10, no. 1, pp. 1–13, Dec. 2020.

[24] O. Rabinovich, I. Kaplon, J. Reis, and A. Epstein, "Experimental demonstration and in-depth investigation of analytically designed anomalous reflection metagratings," *Phys. Rev. B, Condens. Matter*, vol. 99, no. 12, Mar. 2019, Art. no. 125101.

[25] O. Rabinovich and A. Epstein, "Dual-polarized all-metallic metagratings for perfect anomalous reflection," *Phys. Rev. A, Gen. Phys.*, vol. 14, no. 6, Dec. 2020, Art. no. 064028.

[26] T. Hongnara, Y. Shirasawa, T. Sasaki, K. Sasaki, K. Sato, I. Oshima, N. Michishita, H. Nakabayashi, and A. K. Cho, "Dual-polarized broad-beam reflective metasurface based on multi-sheet configuration for local 5G application at 28.25 GHz," in *Proc. 15th Eur. Conf. Antennas Propag. (EuCAP)*, Mar. 2021, pp. 1–4.

[27] V. S. Asadchy, M. Albooyeh, S. N. Tcvetkova, A. Díaz-Rubio, Y. Ra'di, and S. A. Tretyakov, "Perfect control of reflection and refraction using spatially dispersive metasurfaces," *Phys. Rev. B, Condens. Matter*, vol. 94, no. 7, Aug. 2016, Art. no. 075142.

[28] N. M. Estakhri and A. Alù, "Wave-front transformation with gradient metasurfaces," *Phys. Rev. X*, vol. 6, no. 4, Oct. 2016, Art. no. 041008.

[29] G. Gold and K. Helmreich, "A physical surface roughness model and its applications," *IEEE Trans. Microw. Theory Techn.*, vol. 65, no. 10, pp. 3720–3732, Oct. 2017.

[30] K. Lomakin, G. Gold, and K. Helmreich, "Analytical waveguide model precisely predicting loss and delay including surface roughness," *IEEE Trans. Microw. Theory Techn.*, vol. 66, no. 6, pp. 2649–2662, Jun. 2018.

[31] J. Krupka, A. P. Gregory, O. C. Rochard, R. N. Clarke, B. Riddle, and J. Baker-Jarvis, "Uncertainty of complex permittivity measurements by split-post dielectric resonator technique," *J. Eur. Ceram. Soc.*, vol. 21, no. 15, pp. 2673–2676, Dec. 2001.

[32] M. D. Janezic, E. F. Kuester, and J. B. Jarvis, "Broadband complex permittivity measurements of dielectric substrates using a split-cylinder resonator," in *IEEE MTT-S Int. Microw. Symp. Dig.*, vol. 3, Jun. 2004, pp. 1817–1820.

[33] J. Krupka and J. Mazierska, "Contactless measurements of resistivity of semiconductor wafers employing single-post and split-post dielectric-resonator techniques," *IEEE Trans. Instrum. Meas.*, vol. 56, no. 5, pp. 1839–1844, Oct. 2007.

[34] J. Krupka, "Measurements of the complex permittivity of low loss polymers at frequency range from 5 GHz to 50 GHz," *IEEE Microw. Wireless Compon. Lett.*, vol. 26, no. 6, pp. 464–466, Jun. 2016.

[35] H. Kawabata, K.-I. Hasuike, Y. Kobayashi, and Z. Ma, "Multi-frequency measurements of complex permittivity of dielectric plates using higher-order modes of a balanced-type circular disk resonator," in *Proc. Eur. Microw. Conf.*, Sep. 2006, pp. 388–391.

[36] Y. Kato and M. Horibe, "Broadband permittivity measurements up to 170-GHz using balanced-type circular-disk resonator excited by 0.8-mm coaxial line," *IEEE Trans. Instrum. Meas.*, vol. 68, no. 6, pp. 1796–1805, Jun. 2019.

[37] Y. Kato and M. Horibe, "Broadband conductivity measurement technique at millimeter-wave bands using a balanced-type circular disk resonator," *IEEE Trans. Microw. Theory Techn.*, vol. 69, no. 1, pp. 861–873, Jan. 2021.

[38] Y. Kato and M. Horibe, "Broadband complex permittivity and conductivity measurements in the millimeter-wave bands over variable temperatures using a balanced-type circular disk resonator," *Appl. Phys. Lett.*, vol. 119, no. 9, Aug. 2021, Art. no. 092902.

[39] K. U. Inoue, K. Matsui, M. Watanabe, and H. Honma, "Effect of UV irradiation on electroless cu–ni–P plating on cycloolefin polymer," *Trans. IMF*, vol. 87, no. 1, pp. 51–54, Jan. 2009.

[40] A. Epstein and G. V. Eleftheriades, "Synthesis of passive lossless meta-surfaces using auxiliary fields for reflectionless beam splitting and perfect reflection," *Phys. Rev. Lett.*, vol. 117, no. 25, Dec. 2016, Art. no. 256103.

[41] S. D. Targonski and D. M. Pozar, "Minimization of beam squint in microstrip reflectarrays using an offset feed," in *Proc. IEEE Antennas Propag. Soc. Int. Symp.*, vol. 2, Jul. 1996, pp. 1326–1329.

[42] D. K. Ghodgaonkar, V. V. Varadan, and V. K. Varadan, "Free-space measurement of complex permittivity and complex permeability of magnetic materials at microwave frequencies," *IEEE Trans. Instrum. Meas.*, vol. 39, no. 2, pp. 387–394, Apr. 1990.

YUTO KATO (Member, IEEE) received the B.S. and M.S. degrees in physics from The University of Tokyo, Hongo, Japan, in 2010 and 2012, respectively, and the Ph.D. degree from Osaka University, Toyonaka, Japan, in 2020.

Since 2012, he has been with the National Metrology Institute of Japan, National Institute of Advanced Industrial Science and Technology, Tsukuba, Japan. His current research interests include material characterizations and electromagnetic metasurfaces at microwave and millimeter-wave frequencies.
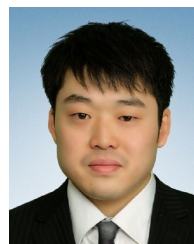
KOHEI OMORI received the B.E. degree from Osaka University, Osaka, Japan, in 2020, where he is currently pursuing the master's degree with the Graduate School of Engineering Science. His current research interests include metasurfaces and metamaterials with exotic electromagnetic properties.

ATSUSHI SANADA (Member, IEEE) received the B.E., M.E., and Ph.D. degrees in electronics engineering from Okayama University, Okayama, Japan, in 1989, 1991, and 1994, respectively.

From 1994 to 1995 and 2002 to 2003, he was a Visiting Scholar with the University of California at Los Angeles, Los Angeles, CA, USA. He was a Visiting Scholar with the Advanced Telecommunications Research Institute International, Seika, Japan, from 2004 to 2005, and Japan Broadcasting Corporation, Tokyo, Japan in 2005. In 2016, he joined the Graduate School of Engineering Science, Osaka University, Osaka, Japan, where he is currently a Professor. His current research interests include microwave science and technologies, including metamaterials, transformation electromagnetics, high-Tc superconducting devices, and ferrite devices.

Dr. Sanada is a member of the European Microwave Association (EuMA) and the Institute of Electronics, Information and Communication Engineers (IEICE), Japan. He has served as an Elected Member for the Administrative Committee of the IEEE Microwave Theory and Techniques Society (MTT-S), from 2015 to 2020, an MTT-S Region 10 Coordinator, from 2011 to 2020, and the Chapter Chair for the MTT-S Kansai Chapter, since 2019.

● ● ●